DOI: 10.1111/nyas.15152

ORIGINAL ARTICLE

ANNALS OF THE NEW YORK ACADEMY OF SCIENCES

Flow sensing on dragonfly wings

Myriam J. Uhrhan[1] | Richard J. Bomphrey[2] | Huai-Ti Lin[1]

[1]Department of Bioengineering, Imperial College London, London, UK

[2]Department of Comparative Biomedical Sciences, Royal Veterinary College, London, UK

Correspondence
Myriam J. Uhrhan and Huai-Ti Lin, Department of Bioengineering, Imperial College London, Exhibition Rd, London SW7 2AZ, UK.
Email: myriam.uhrhan18@imperial.ac.uk and h.lin@imperial.ac.uk

Funding information
Biotechnology and Biological Sciences Research Council, Grant/Award Numbers: BB/R002509/1, BB/R002657/1; Stiftung Begabtenförderung Cusanuswerk

Abstract

One feature of animal wings is their embedded mechanosensory system that can support flight control. Insect wings are particularly interesting as they are highly deformable yet the actuation is limited to the wing base. It is established that strain sensors on insect wings can directly mediate reflexive control; however, little is known about airflow sensing by insect wings. What information can flow sensors capture and how can flow sensing benefit flight control? Here, we use the dragonfly (*Sympetrum striolatum*) as a model to explore the function of wing sensory bristles in the context of flight control. Combining our detailed anatomical reconstructions of both the sensor microstructures and wing architecture, we used computational fluid dynamics simulations to ask the following questions. (1) Are there strategic locations on wings that sample flow for estimating aerodynamically relevant parameters such as the local effective angle of attack? (2) Is the sensory bristle distribution on dragonfly wings optimal for flow sensing? (3) What is the aerodynamic effect of microstructures found near the sensory bristles on dragonfly wings? We discuss the benefits of flow sensing for flexible wings and how the evolved sensor placement affects information encoding.

KEYWORDS
biomechanics, computational fluid dynamics, embodied intelligence, flow sensing, insect flight, morphological computation, wing sensory system

INTRODUCTION

Insect wings can be multifunctional, from being a protective shell to an acoustic instrument,[1,2] and from a visual display to a thermoregulator.[3–5] However, their primary function for flying insects is to produce controlled lift to sustain flight. Just like the wings of vertebrate fliers,[6,7] insect wings are innervated with a network of neurons that form the wing sensory system.[8] What is the role of the wing sensory system in the context of flight control? Unlike the wings of vertebrates, insect wings can only be actuated and controlled at the wing base.[9] This is a great example of an underactuated system in which the degrees of freedom exceed the number of actuators. Despite the lack of actuators on the wings, many insects are still able to produce an impressive variety of flight maneuvers. Dragonflies can accelerate rapidly in any direction as well as hover.[10–13] Furthermore, they perform gliding flight as part of their routine flight repertoire in their natural habitat.[12,14]

Each flight mode comes with different aerodynamic challenges that need to be continuously monitored with high temporal resolution to maintain stable flight. Specifically, the formation and control of the leading-edge vortex has been discussed extensively in the literature, as it can enhance lift by delaying stall.[15,16] In flapping flight, the leading-edge vortex has been identified as a key aerodynamic mechanism that enables the operation of the wing at high angles of attack, during which large lift coefficients can be achieved.[17] During gliding flight, the highly corrugated wings also exhibit regions of recirculation within the

corrugation valleys.[18–21] These slowly rotating trapped vortices form due to flow separation at the sharp vein peaks and reattach at the neighboring downstream vein.[22] Depending on the wing's angle of attack (AoA), the valley vortex system sits within flow separatrices and forms an aerodynamic envelope that more closely resembles the chord profile of a conventional airfoil.[22] The aerodynamic advantage of this arrangement, if any, in terms of lift production and drag reduction is still a source of controversy.[16,18,22–26] Regardless of the verdict, the macrostructure of highly corrugated wings unequivocally impacts the wing's performance.[27,28] During both flapping and gliding flight, insect wings constantly deform as the lightweight wing architecture experiences inertial forces from flapping and aerodynamic forces from the surrounding air.[29–31] This aeroelasticity is an additional factor that further suggests the need of a robust wing sensory system to monitor relevant flight and wing parameters.

While all insect wings possess sensors, dragonfly wings are arguably the most sensorized that have been studied to date.[8,32] The hundreds of sensors on the wing are a physiological investment for the insect as they must be supplied with hemolymph.[33,34] They can be categorized roughly into three classes: strain sensors, flow sensors, and others. Previous work on insect wing sensory systems has mostly focused on strain sensors[35–37] and others.[38,39] In hawkmoths, for example, forcing wing deformation with magnetic perturbation during hovering flight causes consistent shifts in posture that generate torque,[35] demonstrating the importance of wing sensory signals. The existence of campaniform sensilla mechanoreceptors on dipteran halteres are further evidence that the wing sensory system can contribute to flight control. Halteres are vestigial dipteran hindwings that were reduced through evolution; they have lost an aerodynamic function but instead serve as a biological gyroscope to detect body rotations using the retained wing sensory system.[40–43]

To the best of our knowledge no studies have specifically examined how flow sensing on insect wings could benefit flight control. While flow sensors on other body parts have been shown to contribute by, for example, monitoring flow velocities around the head,[44] or by monitoring drag on the antennae,[45,46] little is known about the role of the many flow sensors found on wings.[8,47] The sensory bristles along the wing margin of the silk moth *Bombyx mori* seem to monitor wing beat frequency, and hair sensilla on the wing of the butterfly *Pieris rapae* respond to specific airflow vibration frequencies.[48,49] While this could be functionally relevant to acoustic sensing, the system is also well-suited to monitor the periodic shedding of vortices from the wing. Indeed, the location and coverage of the sensory bristles on the insect wing suggests a possible flow monitoring function.

As the physiological investment of maintaining hundreds of sensors is high,[33,34] the wing sensory system must distribute sensors strategically. What aerodynamic information could the sensors encode at their respective locations in flight? In any wing system, the AoA is the one parameter that directly impacts lift production in both flapping and gliding flight.[16] The one insect that is particularly known for its incredible lift control is the dragonfly, which can even maintain a zero-lift condition in flapping flight.[15] The zero-lift condition needs fine tuning along the whole span, as even slight deviations in wing twist would lead to impediment of zero lift.[15] As dragonflies also spend a lot of time in gliding flight, an obvious assumption is that the high bristle density along the span enables the dragonfly to resolve local AoA, and hence the wing's spanwise load distribution, at least in a steady state. Clearly, monitoring the effective AoA along the wingspan could allow for precise lift control in gliding.

Given a sensory distribution, how the wing sensory system encodes information also depends on the signaling properties of each sensor. Spiking sensory neurons can be broadly categorized into phasic and tonic cells, based on their firing responses.[50,51] While the single-cell characterization of the dragonfly wing mechanosensors are yet to be done, a generic activation model allows us to predict possible ways the system could encode information given the sensor distribution.[52–54] Neural-inspired encoding, using nonlinear activation models, has been successfully implemented to optimize sparse strain sensor placement on flapping wings.[54] While activation models only approximate the neural behavior of a biological system, they are powerful tools to evaluate the readability of a system. Additionally, in the context of the wing sensory system, activation models can be used to compare the evolved sensor placement with randomized sensor locations to explore ideal sensor placement for flow sensing.

In this study, we aim to explore the function of two classes of sensory bristles on dragonfly wings in the context of flow sensing. The first type of bristle lines the wing margin, including the leading edge (Figure 1). They are situated between the serration structures of the leading edge with stereotyped relationships, hence called the *wing margin bristle–bump complex*.[8] The second type of bristle is distributed along the major longitudinal veins at regular intervals. They are all accompanied by a cuticular protrusion/bump; thus, we called them a *bristle–bump complex*.[8] While the second type has only been recently described,[8] the margin bristle–bump complex has long been hypothesized to locally affect the airflow.[55] Here, we will examine the flow over a corrugated dragonfly (*Sympetrum striolatum*) wing section in the context of bristle sensor locations. Additionally, we aim to identify any functional role of the bump or serration structure next to these sensory bristles during gliding flight.

MATERIALS AND METHODS

Innervated hairs of varying length can be found on dragonflies' major longitudinal wing veins.[8] Two short hair sensor types can be found, the wing margin bristle–bump complex at the leading edge and the bristle–bump complex on the posterior longitudinal veins.[8] To investigate the local flow stimulus experienced by these sensors in gliding flight, we made computational fluid dynamics (CFD) models of both sensory bristle types, including the accompanying bump structures, using OpenFOAM 6.0.[56] For the high-resolution 3D models of the sensory complexes, scanning electron microscopy (SEM) images were taken and combined with published confocal data[8] in Blender v3.4.1.[57] We simulated flows similar to, and different from, those expected in gliding flight to calculate forces acting on the bristles under varying

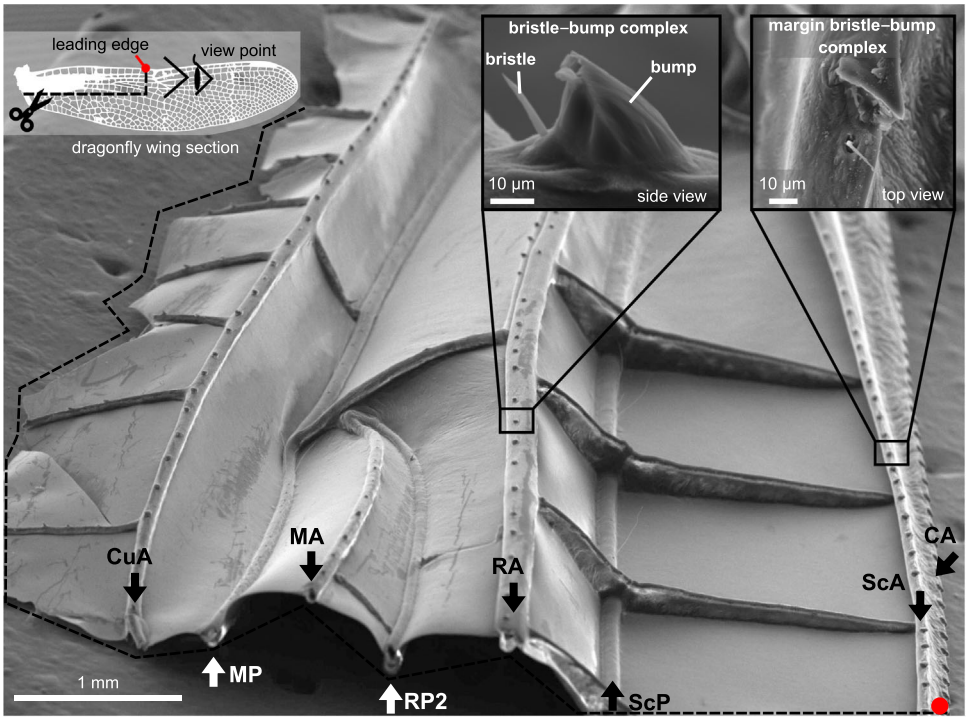

FIGURE 1 Two major flow sensors on the wing of *S. striolatum*. The scanning electron microscopy image of the right forewing shows the eight sensory bristle locations on the corrugated wing indicated by arrows on top of the ridges of the longitudinal veins. Red dot indicates leading edge. The two sensor types analyzed consist of a bump structure next to an innervated short bristle; see insets. Scanning electon microscopy image courtesy of Joseph Fabian for illustration. Abbreviations: CA, costa anterior (ventral leading edge); CuA, cubitus anterior; MA, median anterior; MP, median posterior; RA, radius anterior; RP2, radius posterior; ScA, subcosta anterior (dorsal leading edge); ScP, subcosta posterior.

pitch and yaw flow orientations. The computed forces on the sensory bristles and the surrounding flow fields were assessed in the context of the bump orientation maps made using light microscopy of *Sympetrum striolatum*, the common darter.

(Margin) Bristle–bump complex geometry modeling

Confocal image stacks of the leading-edge (margin) bristle–bump complex and bristle–bump complex of a *S. striolatum* from Ref. 8 were imported into ImageJ.[58] The images were captured using a Zeiss 880 upright confocal microscope (for details see Ref. 8). The stacks were transformed into a 3D iso-surface model, exported in STL format, and loaded into Blender, where the 3D model was smoothed. The model based on confocal data was then aligned with SEM images to confirm the accuracy of the complexes' morphologies. For the SEM images, the forewing of a *S. striolatum* was dried at room temperature and sectioned into two parts to fit in the SEM JSM 5610LV/JSM 6400 (JEOL Ltd). The samples were sputter-coated with gold for 30 s under a 0.003 mbar vacuum. Finally, the SEM data–aligned models were exported as STL files for CFD analysis. To compare the effect of the bump structures, additional reduced leading-edge models and stand-alone bristle models were created.

Cross-section geometry modeling for aerodynamic analyses

To model the aerodynamic forces on the sensory bristles in gliding flight, realistic boundary conditions are vital. Hence, we modeled the sensory structures on the measured cross-section of a dragonfly wing. A high-fidelity 3D model of a *S. striolatum* forewing (ipsilateral pair of hindwings from Ref. 8) was imported into Blender to extract a cross-section model of the dragonfly wing. This forewing model is based on X-ray microtomography (micro-CT) scans of a stained specimen, so some desiccation effects are unavoidable. In our scanned model, the effects could be limited to the trailing edge, which curves downward more than in vivo.[8] In Blender, a slice of the cross-section was subtracted via Boolean operation slightly proximal of the nodus (see Figure 2A). The cross-section was extruded to a thickness of 150 µm, equaling the mean distance between two bristle bump sensors on the radius vein of *S. striolatum*.[8] The model was smoothed and merged with the reconstructed leading edge (wing margin bristle bump and reduced leading-edge model, respectively). The bristle–bump complexes were merged onto their respective vein positions on top of the ridges (Figure 2A). The extruded cross-section model was imported into OpenFOAM, where the fluid domain mesh was generated for CFD.

CFD simulations

CFD simulations were used to compute aerodynamic forces and visualize the flow field around the sensors for varying gliding flight conditions. 2D simulations are often performed due to their advantage in computational cost. In our study, however, where the 3D geometry of the sensor complexes is of particular interest, we chose to perform 3D simulations where the higher accuracy of the results outweighs the additional computational costs (see Methods S1). For the yaw-orientation simulation (azimuth), we approximated the corrugated wing as a flat plane, as modeling the whole wing while resolving the sensor would not be feasible due to the computational costs. Hence, the sensor complexes were modeled as being isolated on a flat plane and compared to stand-alone bristle sensor simulations. For the AoA (wing pitch) simulations, a multiscale approach was taken to model the sensor complexes on the wing. To make the multiscale simulations feasible, a semi-3D approach was taken, where only a small extruded 2D section of the whole wing chord was simulated to reduce the computational cost, while resolving the whole 3D structure of the sensors placed on the extruded section. The 3D simulations were compared to sensor-free 2D cross-section simulations. Residuals and forces from the 2D simulations were analyzed for transient effects, which was the case for simulations >10° AoA (Table S1).

For all cases, OpenFOAM's inbuilt mesh generator *snappyHexMesh* was used to create the meshes consisting of hexahedral and tetrahedral cells. For both yaw (bump orientation) and pitch (AoA) case studies, a cuboidal unstructured mesh domain was created around the wing cross-section and sensor complex within a structured mesh distant to the objects (Figure S1). The unstructured mesh in the vicinity of the test object allows for the discretization of the convoluted wing and sensory structures. To capture the boundary flow physics, mesh refinement boxes and spheres were incorporated around the objects. Additionally, two inflation layers consisting of prismatic cells were added around the walls to ensure that the wall-adjacent cells were parallel to the wall, preventing unphysical boundary effects (Figure S1). Grid independence tests were performed to ensure that the relevant flow features were adequately captured in both the 2D and 3D simulations; mesh sizes and convergence results are shown in Table S2. Following these independence tests, the selected domain sizes were $8C \times 8C \times 0.02C$ (equivalent to 150 μm) for the AoA and $100C \times 40C \times 11C$ for the yaw (bump) orientation study (Figure S2). Force value variation between the medium and the other cases is <5%. Hence, the meshes converged and showed sufficient agreement.

For both pitch (AoA) and yaw (bump orientation) case studies, appropriate boundary conditions were assigned to the domain (Figure S2). At the inlet, a constant velocity magnitude was set (Dirichlet condition). To simulate across AoA in the pitch case studies, the velocity vector at the inlet was changed from −20° to +20°. Here, 0° AoA was based on the geometric angle between the freestream velocity vector and the wing cross-section chord line. For the yaw orientation case study, the velocity vector at the inlet was kept constant at an equivalent to 0° pitch. For both case studies, a pressure-based outlet condition (Neumann) was assigned, with the pressure set to atmospheric pressure. For front and back patches—equivalent to the spanwise direction—of all studies, a cyclic condition was assigned, except for yaw orientation 0° and 180°, where symmetric conditions were set.

A no-slip wall condition was set at the wing and sensory structure surfaces. While the cross-section for the pitch (AoA) study was kept constant, the bristle–bump complex for the yaw study was rotated in 45° intervals to compare forces at varying yaw orientations. For the pitch study, the wing margin bristle bumps and bristle–bump complexes were placed on the cross-section, and for the yaw study, the bristle–bump complex and single bristle sensors were placed on a flat plane approximating the local substrate of the sensor. To rule out the impact of the flat plane boundary, two conditions were compared for the bottom surface of the simulation, no-slip (wall) and slip (freestream) conditions (Figure S3). For the yaw study of the wing margin bristle–bump complex, the leading-edge structure was rotated in 90° steps. For 0° and 180°, equivalent to chordwise flow on the wing, a small section of the membrane posterior to the leading edge was modeled to create realistic boundary conditions (Figure S4). For the 90° orientation—equivalent to spanwise flow on the wing—three different vein boundary conditions were tested to rule out any effect of the boundary conditions on the forces acting on the bristles. The three conditions include no additional vein part, a small vein, and a long vein (see Figure S5). To analyze the impact of the leading-edge bump structure, the same orientations were tested for a leading edge with reduced serration. The final results presented here comprise a set of 29 simulations: seven AoA simulations (−20° to 20°), 14 bristle bump simulations (seven yaw orientations with bump and single bristle), and eight leading-edge simulations (four yaw orientations for the margin bristle–bump complex and the reduced serration model). An overview of all simulations with the respective boundary conditions, numerical approximations, and discretization are listed in Tables S3–S8.

In all simulations, the fluid was considered to be Newtonian and incompressible. The Reynolds number for the pitch (AoA) study was Re = 850, based on the chord length and the notional gliding velocity of 2 ms^{-1} (Ref. 12). The yaw orientation study of the bristle bump and wing margin bristle–bump complex were simulated for a flow of Re = 1.89, using the bump height as the characteristic length. Hence, the flow was modeled steady-state and we observed creeping flow around the sensory complex. For the pitch study, based on the 2D simulations, AoA between −10° and +10° were modeled in steady-state, while higher incidence used a transient simulation to capture flow separation phenomena. For these transient simulations, an appropriate time step was set to reach a quasi-steady solution, where forces oscillate at a constant frequency around a steady value (Figure S6). Flow fields were analyzed in Paraview 5.10.[59] Total aerodynamic forces acting on the bristle sensors and the wing were extracted from the simulations and analyzed in Rstudio 3.4.4.[60]

Sensor location ranking

While the sensor placement on dragonfly wings is restricted to its evolved state, our simulations allow for a more comprehensive analysis of ideal sensor placement. To explore optimal sensor placement for AoA monitoring, we examined chord positions where sensory bristles are absent as well as those locations with sensors in the CFD simulations. To estimate the equivalent aerodynamic forces acting on a sensory bristle at any location we examined on the wing, we established a calibration curve between the forces and the airflow. The relationship was fitted with a linear mixed effect model regression in Rstudio. This enabled us to probe any reference location on the wing as if a sensory bristle was installed. Specific locations included corrugation valleys, the membrane between vein peaks, fore and aft vein peaks, and the trailing edge. The probed airflow was then used to analyze the respective uncertainty-range ratio at each probe location. The probed airflow was further used as direct input for a nonlinear neural activation model to visualize the neural encoded airflow and its readability over AoA.

Uncertainty-range ratio

We ranked the sensor locations based on two parameters: (i) the range of AoA that is injective, meaning the range for which any measured airflow corresponds to only one AoA, and (ii) the robustness of the sensor to noise via the uncertainty influence coefficient. The influence coefficient is a metric for the sensor's sensitivity to noise of the airflow measurements. To determine the injective one-to-one AoA range, we linearly interpolated the computed airflow data points over −20° to +20° AoA. From the resulting dataset, we subtracted all noninjective data points, resulting in a monotonous, injective range of AoA (Figure S7). To calculate the uncertainty influence coefficient, we used the Taylor's series method for uncertainty with a first-order approximation (see Methods S2).[61] We calculated the uncertainty influence coefficient over the whole injective range and took the arithmetic mean. We finally ranked the sensor location via a ratio of uncertainty to one-to-one AoA range. Following our definition of this uncertainty to range ratio, a lower value indicates a better suited location, with high robustness over a wide range of one-to-one AoA.

Neural activation model

To illustrate how the dragonfly could monitor AoA from a set of vein sensors, we built a simple neural activation model. Depending on the rate of adaptation, spiking sensory neurons can be described as tonic or phasic. Tonic cells produce sustained spike trains given the stimulus, and phasic cells produce a fast transient response briefly before returning to a normal state. Both behaviors can be found in the visual and mechanosensory system.[62,63] Following previous studies,[54] we constructed a simple model to predict a potential tonic response of sensory bristles given the aerodynamic results from CFD.

In the tonic cell model, we expect a constant tonic response that changes with stimuli.[50] Depending on the stimulus direction, the firing rate either increases or decreases, hence allowing the encoding of both the stimulus magnitude and direction. Here, we directly used the airflow from sensorized and sensorless reference locations as input. We defined fore–aft flow as positive stimulus and reverse flow as negative stimulus. To predict the firing rate, we used a standard sigmoid activation model[54] that generated both negative and positive outputs (Figure S8). The representative slope of this model was based on experimental data of a wing strain sensor[36] and the threshold (half-max) was parameterized by the best generalized linear model (GLM) fit to predict AoA (Figure S9). The resulting neuron activation rate can be interpreted as neural encoded airflow and was plotted via a heatmap for each location over AoA in Rstudio.

Imaging and bump orientation analysis

To contextualize the computed results of the yaw cases (azimuth) to the actual bump orientation on dragonfly wings, we mapped the orientations of all bumps on two major longitudinal veins of *S. striolatum*. A right forewing dried at room temperature was subsequently bleached in 9% hydrogen peroxide solution for 24 h to increase the contrast between bumps and vein and imaged with a Leica Z6 APO A motorized microscope. Images were postprocessed and stitched together to form a composite wing image in the Leica User Software using the LAS X navigator function. The same samples were prepared and imaged with a confocal microscope as previously described.[8] In imageJ, the *z*-stacks' *z*-projection (along the yaw axis of the wing) of the bristle–bump complexes were stitched together and aligned with the whole wing maps obtained from light microscopy data. From the aligned and *z*-projected confocal images, *x* and *y* position of the bumps' basal front edges were measured (Figure S10). The *z* position was obtained from the confocal *z*-stacks in imageJ. Bump orientations were analyzed in Rstudio and projected on the planforms of the wings in Inkscape 1.01.[64]

RESULTS

AoA sensing

For any wing, the AoA to the airflow is arguably the most important state variable.[65,66] It impacts the lift and drag beneath the stall angle linearly; exceeding the critical angle can result in a dramatic reduction in lift and increase in drag, fluctuating torques, and significant issues maintaining flight control. Even for flapping flight under unsteady conditions, the modulation of AoA (wing pitch) still dictates how the leading-edge vortex[17] is generated, shed, and recaptured.[67] For a rigid wing, the AoA can be determined from the wing base configuration. However, for any flexible wing, the AoA depends on the instantaneous aeroelastic deformation of the wing and cannot rely on

the proprioception at the wing base alone. In this section, we explore how the position of sensory bristles on the dragonfly wings could collectively monitor AoA. We further investigate if the sensor placement on the dragonfly wing is optimal by comparing the sensing capability to other possible positions on the wing. We employed multiscale semi-3D CFD simulations (see Methods) representative of gliding flight. We chose a cross-section at the wingspan location with the highest number of sensorized longitudinal veins (see Figures 1 and 2A). This span location is just proximal to the nodus, a one-way hinge located on the leading edge halfway along the wingspan.[8] According to our previous anatomical work on the sensor map,[8] eight sensor positions can be identified along this specific chord: two rows on the leading edge and on top of the ridges of the six major longitudinal veins (see Figure 2A).[8]

Flow visualization of the wing cross-section confirms expected recirculation within the valleys of the corrugated profile at low AoA (Figure 2B).[22] These small-diameter spanwise vortices appear beneath bounding streamlines that connect one peak to the next along the corrugated profile, enclosing a separation bubble. The wing's lift–drag polar across the full range of AoA (Figure 2C) shows good agreement with previous studies.[18,24,68] Besides the flow field over the cross-section of the wing, the multiscale approach allows for resolving the flow over the microscale sensory bristles at their specific locations. From the CFD simulation, we integrated the aerodynamic pressure and viscous forces on these bristles to obtain the total force acting on each sensory bristle.

Dorsal sensors experience positive fore–aft forces at negative AoA (Figure 2D). As the AoA crosses zero, the leading-edge dorsal sensor experiences a sign reversal of the aerodynamic force as the leading-edge vortex forms. Other sensors experience this reversal sequentially between 5° and 10° as the valley vortices form. A slightly different story is found for the ventral sensors (Figure 2E), as most sensors on the ridges transition to fore–aft flow at −10° already. Apparently, the dorsal valley vortices are not equivalent to those on the ventral side. For the leading-edge ventral sensor, the stagnation point of the entire wing caused a huge signal (Figures 2B inset and 2E).

While the curve progression of force over AoA varies across sensor locations, the force–airflow magnitude relationship is similar (Figure 2F). The fixed airflow with a random sensor location model was tested against a null model with only the random location. The intercept is -0.006 ± 0.01 and the slope is 0.86 ± 0.04. The comparison of the Bayesian information criterion (BIC) indicates that the airflow model (BIC −239) is a better fitting model than the null model (BIC −120). Hence, the airflow magnitude is a good proxy to predict forces acting on the sensory bristle.

To evaluate the locations of these sensory bristles on the wing ridges, we compared the flow at the sensorized positions to some reference positions: at the valleys of the corrugation, at the membrane, at the fore and aft vein peaks, and at the trailing edge (see Figure 2A inset). These reference positions are possible locations where a sensory bristle could exist anatomically but did not. One clear observation is that the flow magnitude is significantly lower in the recirculatory zone of the valleys and other reference locations (Figure 3A). For sensory bristles to sample such small forces, the signal-to-noise ratio would be poor. In fact, ranking the different probe locations via their robustness to one-to-one AoA range ratio shows that the five best probes match sensorized chord locations (Figure 3B). The costa anterior (CA_v) vein at the ventral leading edge has the lowest uncertainty-range ratio and is hence ranked as the most effective sensor location number 1. The CA_v is followed by the other three ventral sensorized locations: subcosta posterior (ScP_v), radius posterior ($RP2_v$), and median posterior (MP_v). Hence, the ventral sensorized vein peak locations are the most effective locations to monitor AoA on this corrugated cross-section.

To explore how sensing local flow magnitude and direction could be used to monitor AoA for stall prevention or for lift prediction, we built a simple neural activation model to visualize the possible signal-encoding patterns (see Methods). Here, we model tonic cell responses where a baseline activity is boosted with stimuli in the preferred direction and suppressed by stimuli in the antipreferred direction (Figure 3A).[50] The chordwise airflow (Figure 3A) from the probes at sensorized and other reference locations (Figure 2A) is the input for the neural activation model. The nonlinear activation function of the model transforms the raw airflow into a normalized neuron activation rate (Figure 3E). Here, we show that, with a tonic activation behavior, the sensory bristles can resolve the AoA over the entire range, as they can continuously encode positive and negative forces (Figure 3E top eight rows). In contrast, sampling flow at other locations could not produce such a clear pattern of activation (Figure 3E), showing a low readability due to the low magnitude of variations. Hence, the readability of the AoA strongly depends on the sensors' span location.

Direction selectivity

The AoA sensing analysis focused on airflow along the chordwise direction. In flight, however, a wing also experiences lateral flow, especially during sideslip conditions. How does the sensory system selectively monitor chordwise flow? The wing sensory bristles modeled in the previous section are all accompanied by one of two possible nearby small cuticular structures. The structures are stereotyped and consistent, as we reported previously.[8] Given the scale of the structure, the leading-edge serration structure has long been hypothesized to affect the local flow.[55] As the newly identified bristle–bump complex is at a same length-scale,[8] we hypothesized that they could modify the local airflow around the sensory bristle and instill direction selectivity to the sensor. To test this hypothesis, we constructed high-fidelity models of (i) the leading-edge serration (Figure 4A) and (ii) the bristle–bump complex (Figure 5A). Then, we simulated the airflow over the sensor complexes from different directions and compared the models with reduced serration/bump and isolated bristle models, respectively (Figures 4A and 5A).

The margin bristle–bump structure and the bristle–bump structure on the longitudinal veins seemingly follow the same orientation. However, the leading edge consists of dorsal and ventral arrays facing the oncoming airflow (Figure 1). The simulations show that the presence of the serration bumps only had a minor reduction of the aerodynamic forces acting on the sensory bristles of around 20% for all but the

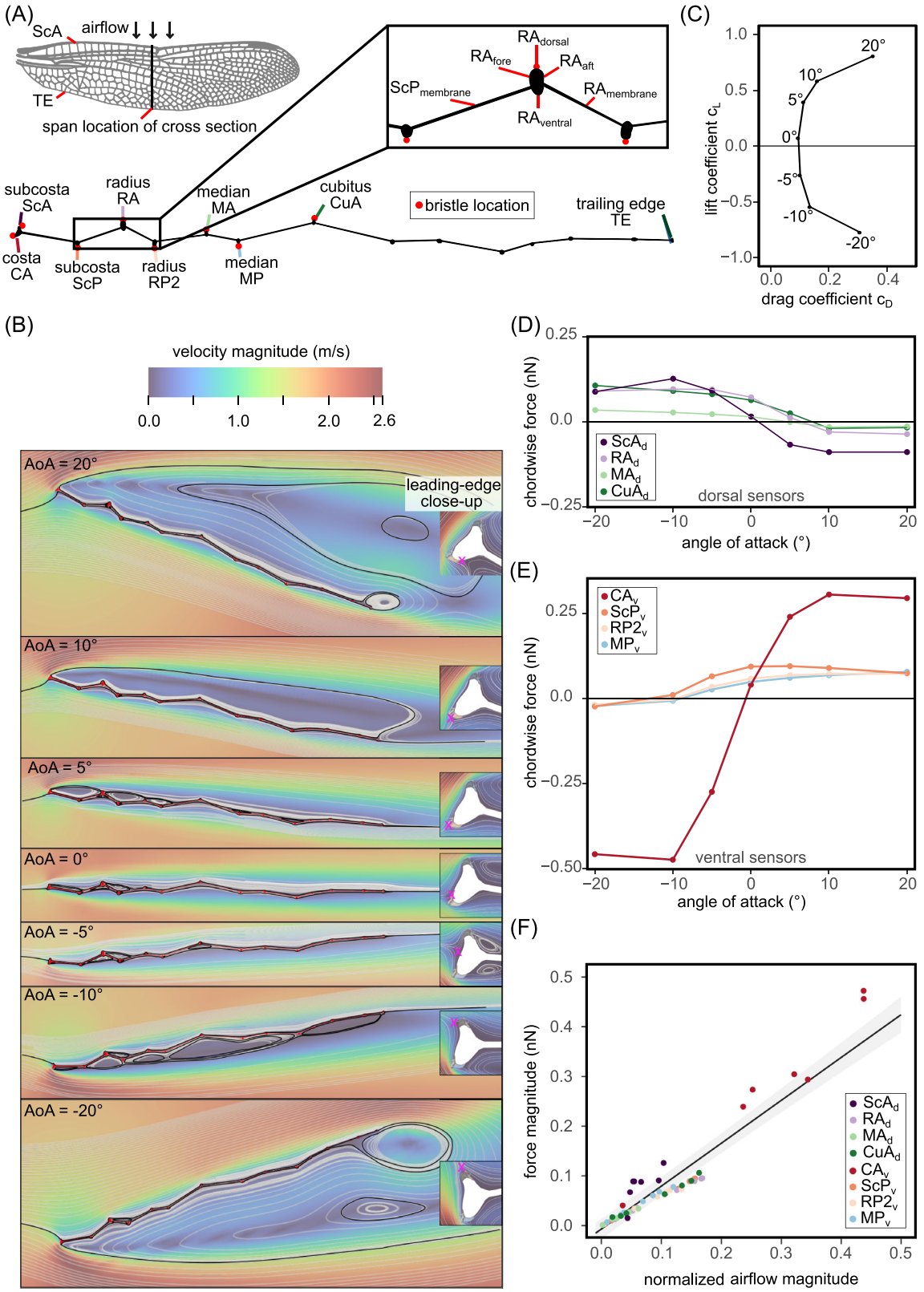

FIGURE 2 Computational fluid dynamic simulation of a wing chord profile of *S. striolatum*. (A) The cross-section of the wing with sensor locations (red circle) and reference (sensorless) probe locations (inset). (B) Flow field (Re = 850) and streamlines over the simulated wing section over varying angles of attack (AoA). The velocity field is color coded by velocity magnitude and streamlines are shown by white and black lines. Transient simulations at AoA ± 20° show time-averaged data. Close-up on leading edge showing stagnation point locations over AoA (purple x). (C) Lift and drag polar of the wing section model. (D) Computed chordwise forces acting on the dorsal sensors over AoA (+ fore–aft flow;−reverse flow). (E) Equivalent computed chordwise forces acting on the ventral sensors. Both dorsal and ventral sensors experience varying force directions

(Continues)

FIGURE 2 (Continued)
and magnitudes over AoA. (F) Computed force magnitude in nN over the respective normalized airflow magnitude for each sensor location (color coded). Black line shows the linear mixed effects model regression, and the gray shaded area shows the 95% confidence interval. CA, costa anterior (ventral leading edge); CuA, cubitus anterior; MA, median anterior; MP, median posterior; RA, radius anterior; RP2, radius posterior; ScA, subcosta anterior (dorsal leading edge); ScP, subcosta posterior; TE, trailing edge.

chordwise flow direction, where no force reduction occurred for the ventral sensor array and 35% for the dorsal array (Figure 4B). However, the leading-edge ventral array is inherently selective to spanwise flow, whereas the dorsal array is mostly sensitive to the chordwise reverse flow, which was not altered by the serration's morphology. A close examination of the local flow demonstrates that the dorsal bump slows down the spanwise flow much better than the ventral bump. The bristle beside the ventral bump is sitting between the ventral and dorsal row in a channel structure running along the leading edge (Figure 4C). Flow arriving at the leading edge can be channeled in the spanwise direction. This pronounced directional selectivity for the leading-edge ventral bristle seems to be the strongest at 0° AoA, where it incidentally reduces the large flow magnitude as shown in Figure 3A.

In contrast to the leading-edge sensors, the longitudinal vein bristle–bump complexes occur in one row on top of the vein ridges. Again, we simulated a high-fidelity configuration with the full bristle–bump complex and another configuration with an isolated bristle (Figure 5A,B). The simulations show the bump slows down the air moving around the bristles to varying degrees depending on the angle of freestream. For both 0° and 180° orientations, the bristle is completely immersed in a slow-moving space surrounding the bump. At 0°, a recirculation area occurs between the bump and bristle sensor; at 180°, the bristle is in the wind shadow of the bump (Figure 5C). These patterns are akin to classical low Reynolds number forward- and backward-facing step tests in fluid mechanics. We can integrate the aerodynamic pressure and viscous forces acting on the entire bristle to estimate total forces. The results show clear minima of forces in the 0° and 180° directions (Figure 5D). While force variations of around 30% are due to the change in projected area of the bristle at varying yaw angles, the introduction of a bump reduces the forces by 85% and 80% for 0° and 180° yaw angle, respectively. Hence, the bump acts as an aerodynamic fence that shields the sensory bristle, conferring a high directional selectivity.

Since directional selectivity can directly impact the input of the sensory bristles for AoA sensing, it follows that any variation in the bump orientation along the wingspan could impact sensitivity to AoA. We measured the bump orientation relative to the bristle on the two major longitudinal veins (subcosta and radius) on the forewing of our study species *S. striolatum* (Figure 5E). On the radius vein, some variation in yaw direction can be observed near the wing base and pterostigma, a highly pigmented spot on the distal part of the leading edge. No orientation shift can be noted for the two adjusting bumps around the nodus. However, at the nodus of *S. striolatum*, there is a distinct gap between sensors. On the subcosta vein, most orientation variation occurs near the nodus. The yaw orientation varies from 50° to 125° along the wingspan. This 50° to 125° bump yaw range implies an airflow variation of up to 30% from the bump orientation alone, based on the force–yaw orientation polar (Figure 5D). These variations impact the respective AoA monitoring function. We can show this impact visually via the neuron activation model introduced in Figure 3C–E. We used a reference bump orientation of 90° to predict the neuron activation rate over AoA for the subcosta and radius vein. Rotating the bump by 45° reduces the airflow at the sensor location by 30%. Comparing the neural activation rate of the manipulated configuration (45°) and the reference configuration (90°) shows different representation of the AoA (Figure 5F). Hence, the readability of the AoA strongly depends on the sensors' location and local flow direction.

DISCUSSION

In this study, we showed that the sensory bristle placement on dragonfly wings allows for monitoring of AoA, at least during the dragonfly's routine gliding flight. The variation in force magnitude and direction over AoA at different chord locations allows for sensor activation patterns that are readable for the nervous system. The readability of AoA strongly depends on the local sensor environment. Shifting the sensing positions only slightly reduces the intensity of the signal. The most effective sensor locations are the ventral vein peaks. Thus, the observed sensor positions are superior to random placement. Besides the sensor placement on the wing, we presented here how the morphological structures in the vicinity of the bristles impact flow sensing. The recently discovered bristle–bump complexes, a sensor type that has only been described on dragonfly wings so far, has an aerodynamic filter function conferring directional selectivity.

Directional selectivity

Using microstructures to shape the local airflow around the sensory bristle is an efficient way to implement directional selectivity. However, inherent directional selectivity has been described previously for insect hair sensors due to material anisotropy or structural asymmetry of the hair shaft or at the hair base.[44,69,70] The 15–25 μm short sensory bristles show no asymmetry of their shaft and have a base aspect ratio of 1.03 ± 0.11 (sample size of $n = 11$, confocal data from Ref. 8). However, since anisotropic material properties at the base have not been investigated for the short bristles on the dragonfly wing,[8] future electrophysiological experiments could confirm if the inherent selectivity exists. The two mechanisms for directional selectivity are not mutually exclusive, and it could be that the inherent selectivity will add to the effects from the bump structures near the bristles. Furthermore, the bump structure also slows down the local flow and has the potential benefit of tuning the flow speed to the range of the sensory bristle. On the wing, the bristle–bumps' orientation varies slightly along the span, but is generally optimal for dampening spanwise flow. This is consistent with the goal of monitoring relevant aerodynamic features since lift-producing mechanisms such as flow circulation and vortex formation mainly occur in the chord direction.[16]

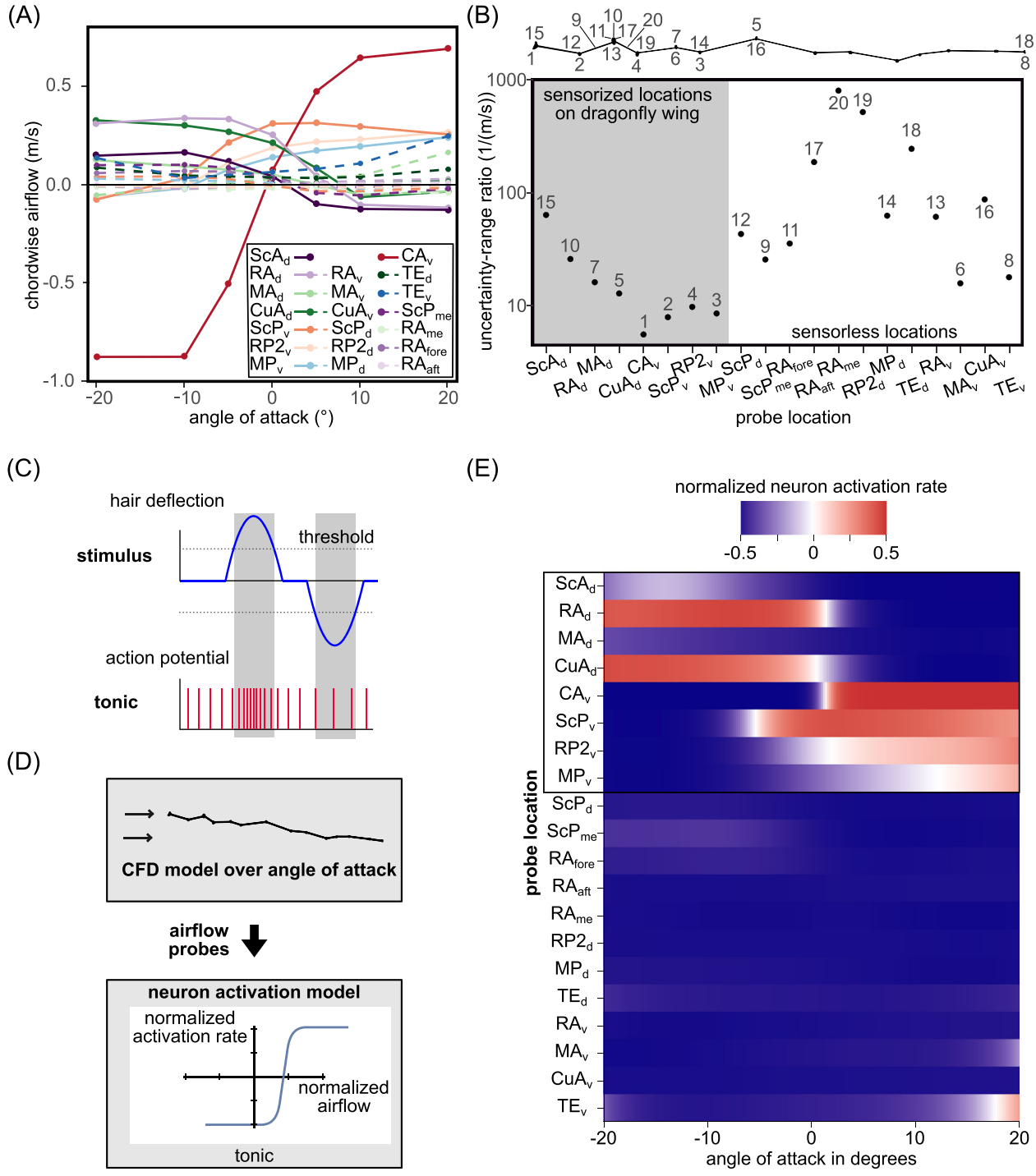

FIGURE 3 Probe locations and neural activation model for angle of attack (AoA) monitoring. (A) Chordwise airflow at sensorized (leading edge and corrugation peaks) and sensorless (trailing edge, corrugation valleys, membrane, and fore/aft vein) spanwise locations. Indices highlighting probe location (d: dorsal; v: ventral; me: membrane). Across the AoA range, the sensorized locations experience visibly larger flow. (B) Uncertainty ratio and resulting position ranking for each probe location. CAv has the lowest uncertainty ratio and is, therefore, ranked number 1 as the most effective sensor location. (C) Neural activation responses of a tonic cell for a theoretical example stimulus based on a nonlinear activation model. (D) Flow chart of the neuron activation model. From CFD simulations, airflow is sampled at varying chord locations. The chordwise airflow is the direct input for the nonlinear neuron activation model. The neuron activation model predicts normalized activation rate of the neurons given the airflow condition at a specific AoA. (E) A heatmap of the normalized tonic neuron activation over AoA show the sensorized chord locations (black rectangle) producing the most meaningful variation with respect to the AoA. Abbreviations: CA_v, costa anterior (ventral); CuA_d, cubitus anterior (dorsal); CuA_v, cubitus anterior (ventral); MA_d, median anterior (dorsal); MA_v, median anterior (ventral); MP_d, median posterior (dorsal); MP_v, median posterior (ventral); RA_{aft}, radius anterior (aft); RA_d, radius anterior (dorsal); RA_{fore}, radius anterior (fore); RA_{me}, radius anterior (membrane); RA_v, radius anterior (ventral); $RP2_d$, radius posterior (dorsal); $RP2_v$, radius posterior (ventral); ScA_d, subcosta anterior (dorsal); ScP_d, subcosta posterior (dorsal); ScP_{mem}, subcosta posterior (membrane); ScP_v, subcosta posterior (ventral); TE_d, trailing edge (dorsal); TE_v, trailing edge (ventral).

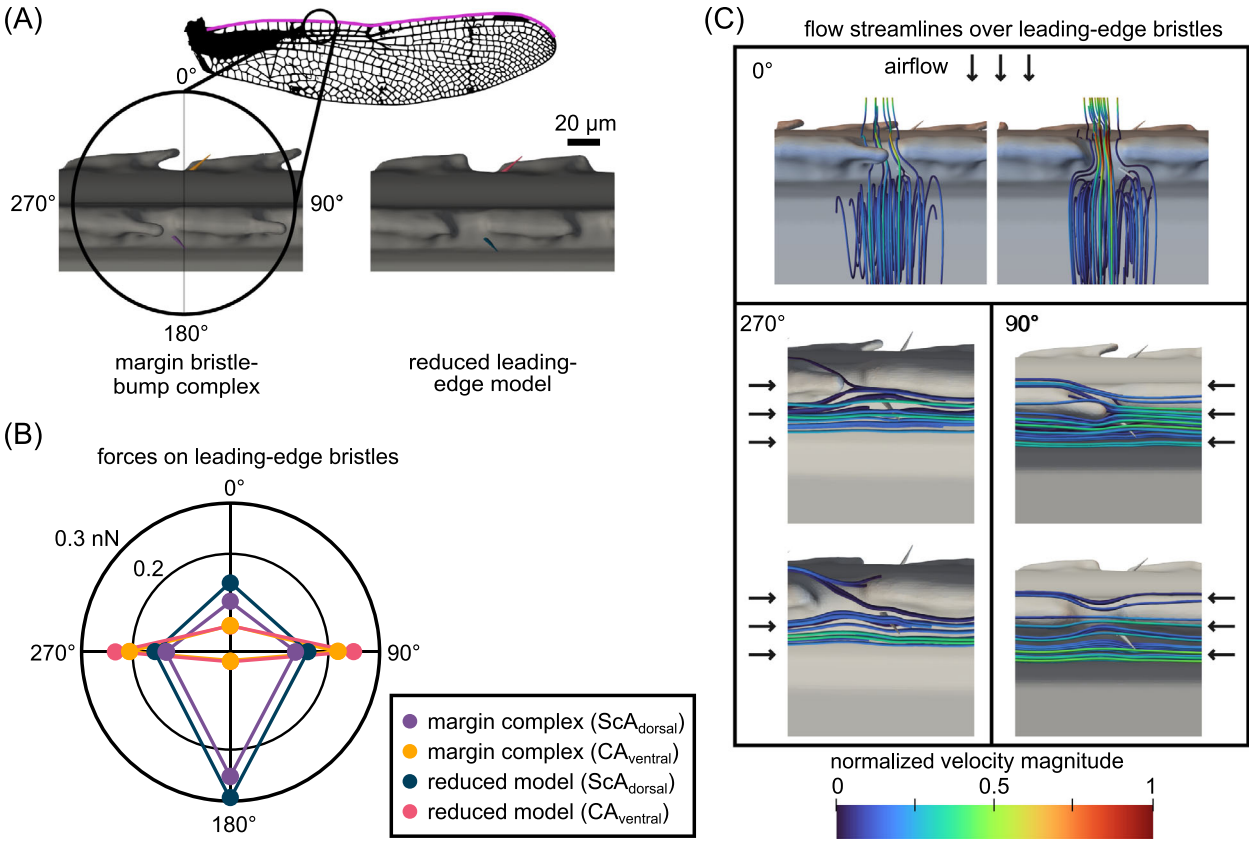

FIGURE 4 Direction selectivity of the wing margin bristle–bump complex: Computational fluid dynamic simulation at Re = 2. (A) Structural 3D models of the wing margin bristle–bump complex (left) and the reduced serration model (right). (B) Total aerodynamic forces acting on the leading-edge sensors over yaw angles at 0° AoA (pitch). An inherent direction selectivity for both dorsal and ventral sensor arrays is demonstrated, with the dorsal sensors being most sensitive to chordwise reverse flow and the ventral sensors being selective to spanwise flow. The bump structure reduces the aerodynamic forces for all but the chordwise flow direction, where no filtering occurs for the ventral sensors and increased filtering occurs for the dorsal sensors. (C) Top view of the flow streamlines around the leading-edge sensors. Streamlines are color coded by normalized velocity magnitude. Fore–aft flow: 0°, reverse flow 180°, spanwise flow: 90° and 270°. The dorsal bristle is shielded by its neighboring bump structure. The ventral bristle sits between the dorsal and ventral bump row. Abbreviations: CA, costa anterior; ScA, subcosta anterior.

Flow readability

Based on our simple neural activation model, the sensor tuning could impact the resolution and encoding of the local effective AoA. In the tonic cell model, each sensor accounts for both the airflow direction and magnitude. For the representative model parameters here, the sensor system of the dragonfly can resolve the entire range of AoA (−20° to +20°). However, to resolve the whole range, not all eight sensor locations are needed. The median anterior (MA$_d$) vein shows only a minor change in activation rate and is not contributing to the readability of the AoA. The MA$_d$ vein is in the wind shadow of the higher radius anterior (RA) peak, resulting in lower flow magnitude and flow range over AoA. Hence, to resolve the whole range of AoA, only seven sensor locations are required.

Besides the model and its parameters, the sensor input value strongly affects the readability of the system. While the model and exact parameters depend on the neurophysiology of the system, the sensor input varies with the sensor location on the corrugated wing section. The highest signals and signal range occur on top of the vein peaks and even slight shifts away from the peaks of the veins result in a lower signal, hence reducing the readability of the sensor. Due to the varying flow–AoA curves for each sensor location, differences in robustness and one-to-one AoA ranges occur. Low-reliability locations are around the dorsal valley of the radius RP2 vein and most sensorized locations are well-suited except the dorsal leading edge of the subcosta anterior (ScA$_d$). This exception is likely due to margin bump altering the airflow around the sensor, leading to a comparatively small one-to-one AoA range at the ScA$_d$. The sensor locations on the ventral peaks are the most effective locations to monitor AoA, as they have the lowest uncertainty to one-to-one AoA range ratio. On the dragonfly wing, the sensory bristles are exactly located at these ideal locations. Thus, the system is efficiently sampling the flow, highlighting the embodied intelligence of the wing sensory system.

Implications for flight control

In steady-state conditions, monitoring the effective AoA gives the insect a proxy for the lift and drag forces being generated.[71]

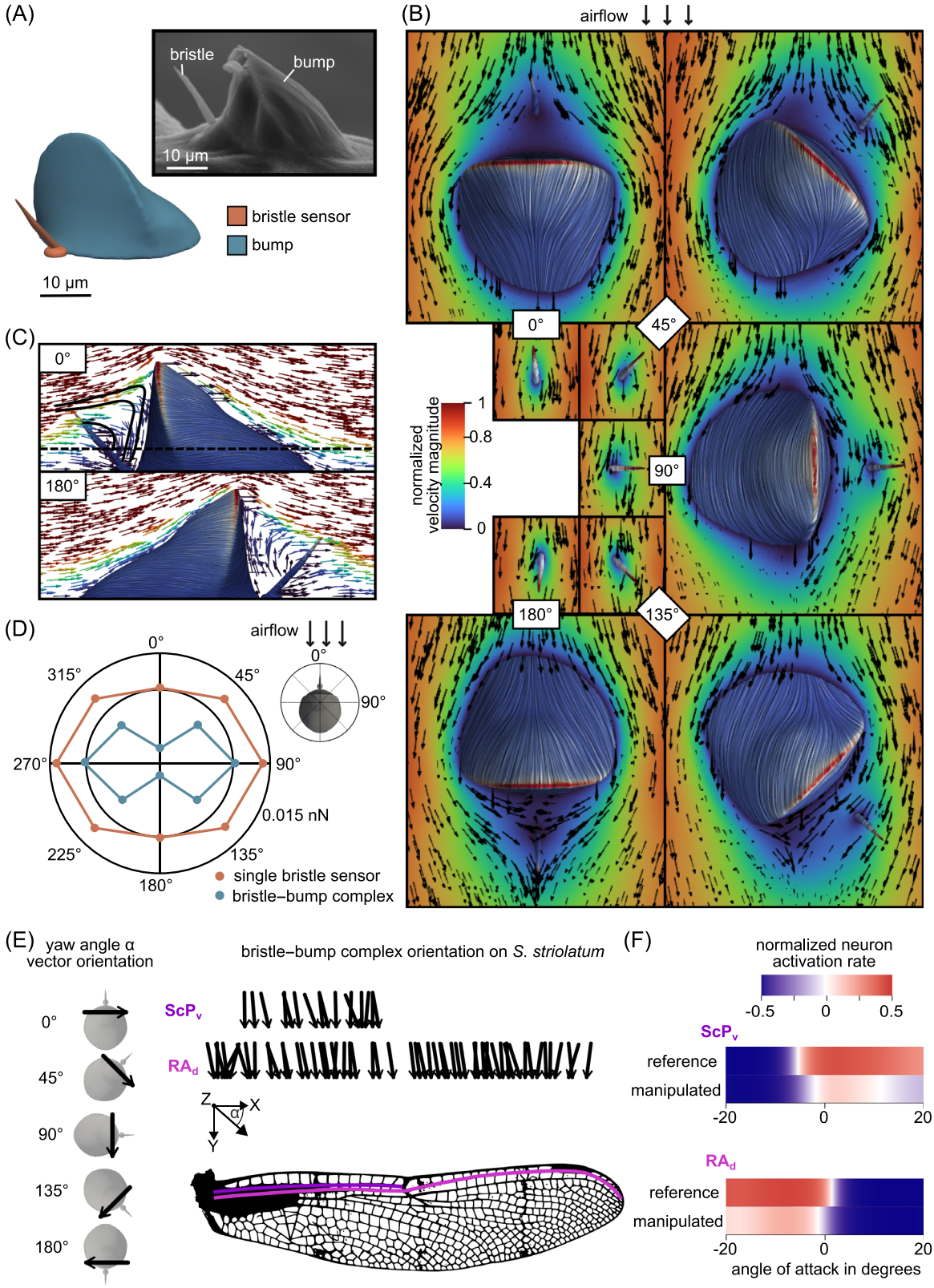

FIGURE 5 Direction selectivity and orientation of the bristle–bump complex: Computational fluid dynamic simulation at Re = 2. (A) Structural 3D model of the bristle–bump complex. Inset shows scanning electron microscopy image of a bristle–bump complex on the radius vein of *S. striolatum*. (B) Top view of horizontal flow fields over the bristle–bump complex (outer figures) and single bristle sensors (inner figures). The flow field is color coded by normalized velocity magnitude, with arrows indicating flow vector orientation. The height of the horizontal flow field is highlighted by a dotted line in C. The bump slows down the fluid in its vicinity. (C) Vertical flow field of 0° and 180°. Black lines highlight recirculation area between bristle and bump at 0°. (D) Total aerodynamic forces acting on the sensors for single bristle and bristle–bump complex

(Continues)

FIGURE 5 (Continued)
over varying yaw orientations. The presence of the bump reduces forces over all yaw angles and confers a direction selectivity due to the higher filtering in 0° and 180° orientation. (E) Preferred flow-sensing direction (equivalent to 90° in panel B) of bristle–bump complexes on two longitudinal veins (ScP and Ra) on a *S. striolatum* forewing. The arrow direction is based on the bump's orientation on the wing measured along the span of the two veins. The *x*-coordinate of the arrows indicate bump spanwise location on the wing. Pitch orientation of the bump varies only slightly between $\pm$ 2° and is not shown. Yaw orientation varies between 50° and 125° along the wingspan. Left: Yaw orientation legend. (F) Activation patterns over AoA given a 45° rotation of the bump on subcosta posterior (ScP) and radius anterior (RA). The reference configuration corresponds to a bump orientation of 90°. If the bump was rotated by 45°, the input airflow would be reduced by 30%, leading to a different representation of the AoA. Abbreviation: AoA, angle of attack.

Knowledge of the effective AoA along the span can increase the accuracy of lift estimates regardless of the wing deformation due to aeroelastic loads during flight[72,73] or the ipsilateral wing pair interaction.[16] While we only evaluate the system in the steady state, the strategic locations of these flow sensors should be able to capture AoA information during flapping flight as well, perhaps with a different encoding format. How the nervous system interprets the signals from the same set of sensors in these two flight modes would be an interesting research question.

We have shown that the flow sensors could monitor the location of the recirculation bubble separation and reattachment lines because they give rise to changing local flow orientations. As the reattachment line moves back along the wing chord, flow vector directions can shift by up to 180°. The combined information of the sensors in a chordwise direction allows the estimation of the size of the laminar separation bubble during gliding flight and likely the leading-edge vortex during flapping flight. These are both key aerodynamic features during high-lift flapping flight that build up once per stroke cycle.[17,74] Like campaniform sensilla that fire once per flapping cycle due to cuticular strain,[75] sensory bristles could capture the vortex formation each flapping cycle. Hence, mechanosensory feedback can be used to control vortex evolution in real-time, allowing the insect to rapidly adjust their wing pitch to initiate formation, growth, stabilization, or shedding of vortices as needed. For this application, the directional selectivity of the sensory bristles would be crucial.

Another critical parameter for lift control and especially wing stall prevention is stagnation monitoring. Even in gliding flight, aeroelastic deformation (e.g., wing bending and twisting) can occur suddenly, leading to fast changes in the spanwise load. This could cause unfavorable wing divergence, where high lift at the wing tip and wing twist feedback positively, ultimately leading to tip stall or even structural damage.[76,77] The double rows of leading-edge sensors could be a good solution for high-accuracy stagnation sensing around the zero-lift condition. Changes in AoA, and hence lift, are coupled with movement of the stagnation point location; as such, the wing margin bristle–bump complexes are at the ideal location to monitor shifts in the stagnation line around the leading edge.[55] Based on the flow direction at those sensors, the insect could localize the stagnation point to be either between the two rows, dorsal, or ventral, corresponding to near-zero lift, negative lift, or positive lift, respectively.

Study limitations and ongoing work

The study we present here is not without some limitations. First, some of our CFD simulations performed fall in the transitional range of the Knudsen number.[78] The simulations of isolated bristles are at Kn = 0.032 (hair diameter D = 2×10^{-6} m and free mean path of air at room temperature $\lambda = 6.544 \times 10^{-8}$ m)[79] and fall in the low slip flow region, where gas molecules' interaction with walls become more prominent. Future simulations could implement a Maxwell slip model to quantify the boundary effects. A second limitation relates to the wing cross-sectional model. While the leading edge is reinforced and robust to contrast staining for X-ray microtomography scanning, the trailing edge is more delicate and exhibited small additional curvature due to desiccation during preparation. Aeroelastic bending of the wing has been neglected in our simulations and the cross-section has been assumed to be rigid and static, which in reality is unlikely to be the case. The impact of wing bending on the flow field could be addressed with an ongoing fluid–structure interaction (FSI) simulation. Periodic deformation (flutter or buffeting) would make the airflow strongly time-dependent. Ongoing modeling work resolves structural changes using coupled physics simulations and will consider transient phenomena at all AoA. While the semi-3D approach allowed for multiscale flow analyses and local force measurements, it likely underestimates spanwise flows that frequently occur in both flapping and gliding flight.[16] To capture a realistic flow field over insect wings, a high-fidelity 3D wing model has been built and is being evaluated. Finally, the bump orientation map is based on a single dragonfly species. A cross-species comparison of bump orientation will provide critical insight into flow sensing in dragonflies with different flight behaviors.

CONCLUDING REMARKS

In summary, applying a neural activation model to our CFD simulations shows that a small number of flow-sensing bristles placed on the corrugation wing ridges would capture key aerodynamic features relevant to gliding flight. In contrast to other locations on the wing, the bristle sensors' locations on the ridges are ideal to monitor: (1) lift via the effective AoA; (2) the stagnation point; and (3) the laminar separation bubble at high AoA. Furthermore, bumps in the bristle–bump complex

are not innervated but impose selectivity to chordwise flow for the sensory bristles. In contrast, the serration spikes at the leading edge reduce the flow magnitude for the leading-edge bristles only slightly. Nevertheless, the spike geometry causes the dorsal row to have a selective preference for reverse chordwise flow and the ventral row for spanwise flow. Finally, we report variation of the bump orientation on the subcostal and radius veins along the wingspan. This variation will impact sensing along the wingspan across regions where chord profile and fore–aft sweep angle are also variable. Hence, the bristle–bump complex on dragonfly wings is an example of embodied intelligence, or morphological computing, since the physical structure acts as a mechanical filter, reducing the complexity of the signal reaching the controller.

The idea of using wing-mounted sensors to inform a flight controller has gained popular attention in recent years. While some have approached it from an engineering perspective, others have studied the wing sensory systems of flying animals directly.[6,66,80] Most of the animal work focuses on the relationship between wing morphing and the associated deformation sensing. Here, we argue that flow sensing provides a different type of information. Direct flow sensing on wings allows for rapid prediction of the instantaneous lift and AoA, as well as detecting the onset of stall. While wing deformation can be driven by a variety of aeroelastic mechanisms in flight (i.e., the fine interplay of inertial effects and FSIs), the signals from flow sensors continuously predict aerodynamic state. This is especially important during fast nonlinear transitions of flight mode or when experiencing external perturbations such as gusts. Here, we present a neuron activation model serving as a framework and analysis pipeline applicable for ongoing and future work on 3D unsteady, flapping analysis given the wing sensory system. We expect direct flow sensing on wings will enable comprehensive monitoring of nonlinear aerodynamic phenomena, increasing both flight safety and aerodynamic efficiency.

AUTHOR CONTRIBUTIONS

M.J.U., R.J.B., and H-T.L. conceptualized the work. M.J.U. and H-T.L. developed the methodology and performed the work with input from R.J.B. H-T.L. supervised the project and M.J.U. performed all analyses. M.J.U. and H-T.L. wrote the original draft. M.J.U., R.J.B., and H-T.L. reviewed and edited the final manuscript.

ACKNOWLEDGEMENTS

This study was supported by a Cusanuswerk scholarship (M.J.U.) and by Biotechnology and Biological Sciences Research Council grants BB/R002509/1 (H-T.L.) and BB/R002657/1 (R.J.B.). The authors thank Igor Siwanowicz for providing confocal data of the leading edge from previously published work.[8] We thank Masateru Maeda for providing the forewing model of *S. striolatum* from which we extracted a cross-section. We thank Joseph Fabian for providing SEM images for illustration and modeling. We thank Ben Campbell for discussion on uncertainty propagation and sensor robustness. We thank Alexandra Yarger for discussion on insect wing sensory system and Rafael Palacios for conversations about wing aeroelastic effects. We also thank other members of the Neuromechanics & Bioinspired Technologies (Lin) Lab for feedback during lab meetings.

COMPETING INTERESTS

The authors declare no competing interests.

ORCID

Myriam J. Uhrhan https://orcid.org/0000-0003-3071-6555
Richard J. Bomphrey https://orcid.org/0000-0002-4748-0510
Huai-Ti Lin https://orcid.org/0000-0003-3370-244X

PEER REVIEW

The peer review history for this article is available at: https://publons.com/publon/10.1111/nyas.15152

REFERENCES

1. Xing, Y., & Yang, J. (2020). Stiffness distribution in natural insect cuticle reveals an impact resistance strategy. *Journal of Biomechanics*, *109*, 109952. https://doi.org/10.1016/j.jbiomech.2020.109952
2. Clark, C. J. (2021). Ways that animal wings produce sound. *Integrative and Comparative Biology*, *61*(2), 696–709. https://doi.org/10.1093/icb/icab008
3. Théry, M., & Gomez, D. (2010). Insect colours and visual appearance in the eyes of their predators. *Advances in Insect Physiology*, *38*(C), 267–353. https://doi.org/10.1016/S0065-2806(10)38001-5
4. Guillermo-Ferreira, R., Bispo, P. C., Appel, E., Kovalev, A., & Gorb, S. N. (2015). Mechanism of the wing colouration in the dragonfly *Zenithoptera lanei* (Odonata: Libellulidae) and its role in intraspecific communication. *Journal of Insect Physiology*, *81*, 129–136. https://doi.org/10.1016/j.jinsphys.2015.07.010
5. Tsai, C. C., Childers, R. A., Nan Shi, N., Ren, C., Pelaez, J. N., Bernard, G. D., Pierce, N. E., & Yu, N. (2020). Physical and behavioral adaptations to prevent overheating of the living wings of butterflies. *Nature Communications*, *11*(1), 551. https://doi.org/10.1038/s41467-020-14408-8
6. Rummel, A. D., Sierra, M. M., Quinn, B. L., & Swartz, S. M. (2023). Hair, there and everywhere: A comparison of bat wing sensory hair distribution. *Anatomical Record*, *306*(11), 2681–2692. https://doi.org/10.1002/ar.25176
7. Brown, R. E., & Fedde, M. R (1993). Airflow sensors in the avian wing. *Journal of Experimental Biology*, *179*(1), 13–30. https://doi.org/10.1242/jeb.179.1.13
8. Fabian, J., Siwanowicz, I., Uhrhan, M., Maeda, M., Bomphrey, R. J., & Lin, H.-T. (2022). Systematic characterization of wing mechanosensors that monitor airflow and wing deformations. *Iscience*, *25*(4), 104150. https://doi.org/10.1016/j.isci.2022.104150
9. Hatch, G. (1966). Structure and mechanics of the dragonfly pterothorax. *Annals of the Entomological Society of America*, *59*(4), 702–714. https://doi.org/10.1093/aesa/59.4.702
10. Azuma, B. Y. A., & Watanabe, T. (1988). Flight performance of a dragonfly. *Journal of Experimental Biology*, *137*(1), 221–252.
11. Rüppell, G. (1989). Kinematic analysis of symmetrical flight manoeuvres of odonata. *Journal of Experimental Biology*, *144*(1), 13–42.
12. Wakeling, J. M., & Ellington, C. P. (1997). Dragonfly flight: I gliding flight and steady-state aerodynamic forces. *Journal of Experimental Biology*, *200*(3), 543–556. https://doi.org/10.1242/jeb.200.3.543
13. Wakeling, J. M., & Ellington, C. P. (1997). Dragonfly flight II. Velocities, accelerations and kinematics of flapping flight. *Journal of Experimental Biology*, *200*, 557–582.

14. May, M. L. (1982). Heat exchange and endothermy in protodonata. *Evolution; International Journal of Organic Evolution*, *36*(5), 1051. https://doi.org/10.2307/2408082
15. Thomas, A. L. R., Taylor, G. K., Srygley, R. B., Nudds, R. L., & Bomphrey, R. J. (2004). Dragonfly flight: Free-flight and tethered flow visualizations reveal a diverse array of unsteady lift-generating mechanisms, controlled primarily via angle of attack. *Journal of Experimental Biology*, *207*(24), 4299–4323. https://doi.org/10.1242/jeb.01262
16. Bomphrey, R. J., Nakata, T., Henningsson, P., & Lin, H.-T. (2016). Flight of the dragonflies and damselflies. *Philosophical Transactions of the Royal Society B: Biological Sciences*, *371*(1704), 20150389. https://doi.org/10.1098/rstb.2015.0389
17. Ellington, C. P., Van Den Berg, C., Willmott, A. P., & Thomas, A. L. R. (1996). Leading-edge vortices in insect flight. *Nature*, *384*(6610), 626–630. https://doi.org/10.1038/384626a0
18. Kesel, A. B. (2000). Aerodynamic characteristics of dragonfly wing sections compared with technical aerofoils. *Journal of Experimental Biology*, *203*(20), 3125–3135.
19. Kim, W. K., Ko, J. H., Park, H. C., & Byun, D. (2009). Effects of corrugation of the dragonfly wing on gliding performance. *Journal of Theoretical Biology*, *260*(4), 523–530. https://doi.org/10.1016/j.jtbi.2009.07.015
20. Flint, T. J., Jermy, M. C., New, T. H., & Ho, W. H. (2017). Computational study of a pitching bio-inspired corrugated airfoil. *International Journal of Heat and Fluid Flow*, *65*, 328–341. https://doi.org/10.1016/j.ijheatfluidflow.2016.12.009
21. Krishna, S., Cho, M., Wehmann, H. N., Engels, T., & Lehmann, F. O. (2020). Wing design in flies: Properties and aerodynamic function. *Insects*, *11*(8), 466. https://doi.org/10.3390/insects11080466
22. Vargas, A., Mittal, R., & Dong, H. (2008). A computational study of the aerodynamic performance of a dragonfly wing section in gliding flight. *Bioinspiration & Biomimetics*, *3*(2), 26004. https://doi.org/10.1088/1748-3182/3/2/026004
23. Rees, C. J. C. (1975). Form and function in corrugated insect wings. *Nature*, *256*(5514), 200–203. https://doi.org/10.1038/256200a0
24. Rudolph, R. (1978). Aerodynamic properties of *Libellula quadrimaculata* L. (Anisoptera: Libellulidae), and the flow around smooth and corrugated wing section models during gliding flight. *Odonatologica*, *7*(I), 49–58.
25. Obata, A., & Sinohara, S. (2009). Flow visualization study of the aerodynamics of modeled dragonfly wings. *AIAA Journal*, *47*(12), 3043–3046. https://doi.org/10.2514/1.43836
26. Fujita, Y., & Iima, M. (2023). Dynamic lift enhancement mechanism of dragonfly wing model by vortex–corrugation interaction. *Physical Review Fluids*, *8*(12), 123101. https://doi.org/10.1103/PhysRevFluids.8.123101
27. Young, J., Walker, S. M., Bomphrey, R. J., Taylor, G. K., & Thomas, A. L. R. (2009). Details of insect wing design and deformation enhance aerodynamic function and flight efficiency. *Science*, *325*(5947), 1549–1552. https://doi.org/10.1126/science.1175928
28. Zhang, Z., Yin, Y., Zhong, Z., & Zhao, H. (2015). Aerodynamic performance of dragonfly wing with well-designed corrugated section in gliding flight. *Computer Modeling in Engineering and Sciences*, *109*(3), 285–302.
29. Combes, S. A., & Daniel, T. L. (2003). Into thin air: Contributions of aerodynamic and inertial-elastic forces to wing bending in the hawkmoth *Manduca sexta*. *Journal of Experimental Biology*, *206*(17), 2999–3006. https://doi.org/10.1242/jeb.00502
30. Rajabi, H., & Gorb, S. N. (2020). How do dragonfly wings work? A brief guide to functional roles of wing structural components. *International Journal of Odonatology*, *23*(1), 23–30. https://doi.org/10.1080/13887890.2019.1677515
31. Kesel, A. B., Philippi, U., & Nachtigall, W. (1998). Biomechanical aspects of the insect wing: An analysis using the finite element method. *Computers in Biology and Medicine*, *28*(4), 423–437. https://doi.org/10.1016/S0010-4825(98)00018-3
32. Aiello, B. R., Stanchak, K. E., Weber, A. I., Deora, T., Sponberg, S., & Brunton, B. W. (2021). Spatial distribution of campaniform sensilla mechanosensors on wings: Form, function, and phylogeny. *Current Opinion in Insect Science*, *48*, 8–17. https://doi.org/10.1016/j.cois.2021.06.002
33. Arnold, J. W. (1964). Blood circulation in insect wings. *Canadian Entomologist*, *96*(1–2), 98.
34. Guillermo-Ferreira, R., Appel, E., Urban, P., Bispo, P. C., & Gorb, S. N. (2017). The unusual tracheal system within the wing membrane of a dragonfly. *Biology Letters*, *13*(5), 20160960. https://doi.org/10.1098/rsbl.2016.0960
35. Dickerson, B. H., Aldworth, Z. N., & Daniel, T. L. (2014). Control of moth flight posture is mediated by wing mechanosensory feedback. *Journal of Experimental Biology*, *217*(13), 2301–2308. https://doi.org/10.1242/jeb.103770
36. Pratt, B., Deora, T., Mohren, T., & Daniel, T. (2017). Neural evidence supports a dual sensory-motor role for insect wings. *Proceedings of the Royal Society B: Biological Sciences*, *284*(1862), 20170969. https://doi.org/10.1098/rspb.2017.0969
37. Dickinson, M. H. (1990). Linear and nonlinear encoding properties of an identified mechanoreceptor on the fly wing measured with mechanical noise stimuli. *Journal of Experimental Biology*, *151*, 219–244.
38. Houot, B., Gigot, V., Robichon, A., & Ferveur, J. F. (2017). Free flight odor tracking in Drosophila: Effect of wing chemosensors, sex and pheromonal gene regulation. *Scientific Reports*, *7*(1), 40221. https://doi.org/10.1038/srep40221
39. Li, J., Zhang, W., Guo, Z., Wu, S., Jan, L. Y., & Jan, Y. N. (2016). A defensive kicking behavior in response to mechanical stimuli mediated by Drosophila wing margin bristles. *Journal of Neuroscience*, *36*(44), 11275–11282. https://doi.org/10.1523/JNEUROSCI.1416-16.2016
40. Yarger, A. M., & Fox, J. L. (2016). Dipteran halteres: Perspectives on function and integration for a unique sensory organ. *Integrative and Comparative Biology*, *56*(5), 865–876. https://doi.org/10.1093/icb/icw086
41. Fox, J. L., Fairhall, A. L., & Daniel, T. L. (2010). Encoding properties of haltere neurons enable motion feature detection in a biological gyroscope. *Proceedings of the National Academy of Sciences of the United States of America*, *107*(8), 3840–3845. https://doi.org/10.1073/PNAS.0912548107
42. Dickinson, M. H. (1999). Haltere–mediated equilibrium reflexes of the fruit fly, *Drosophila melanogaster*. *Philosophical Transactions of the Royal Society of London. Series B: Biological Sciences*, *354*(1385), 903–916. https://doi.org/10.1098/rstb.1999.0442
43. Pringle, J. (1948). The gyroscopic mechanism of the halteres of Diptera. *Philosophical Transactions of the Royal Society of London. Series B, Biological Sciences*, *233*(602), 347–384. https://doi.org/10.1098/rstb.1948.0007
44. Camhi, J. M. (1969). Locust wind receptors. I. Transducer mechanics and sensory response. *Journal of Experimental Biology*, *50*(2), 335–348.
45. Taylor, G., Bomphrey, R., & 't Hoen, J. (2006). Insect flight dynamics and control. 44th AIAA Aerospace Sciences Meeting and Exhibit. https://doi.org/10.2514/6.2006-32
46. Gewecke, M. (1970). Antennae: Another wind-sensitive receptor in locusts. *Nature*, *225*(5239), 1263–1264. https://doi.org/10.1038/2251263a0
47. Altman, J. S., Anselment, E., & Kutsch, W. (1978). Postembryonic development of an insect sensory system: Ingrowth of axons from hindwing sense organs in *Locusta migratoria*. *Proceedings of the Royal Society of London—Biological Sciences*, *202*(1149), 497–516. https://doi.org/10.1098/rspb.1978.0082
48. Ai, H., Yoshida, A., & Yokohari, F. (2010). Vibration receptive sensilla on the wing margins of the silkworm moth *Bombyx mori*. *Journal of Insect Physiology*, *56*(3), 236–246. https://doi.org/10.1016/j.jinsphys.2009.10.007

49. Yoshida, A., Noda, A., & Emoto, J. (2001). Bristle distribution along the wing margin of the small white cabbage butterfly (Lepidoptera: Pieridae). *Annals of the Entomological Society of America*, *94*(3), 467–470. https://doi.org/10.1603/0013-8746(2001)094[0467:BDATWM]2.0.CO;2
50. Pearson, K. G., & Rowell, C. H. F. (1977). Functions of tonic sensory input in insects. *Annals of the New York Academy of Sciences*, *290*(1), 114–123. https://doi.org/10.1111/j.1749-6632.1977.tb39721.x
51. Frye, M. A. (2001). Encoding properties of the wing hinge stretch receptor in the hawkmoth *Manduca sexta*. *Journal of Experimental Biology*, *204*(21), 3693–3702. https://doi.org/10.1242/jeb.204.21.3693
52. Aljadeff, J., Lansdell, B. J., Fairhall, A. L., & Kleinfeld, D. (2016). Analysis of neuronal spike trains, deconstructed. *Neuron*, *91*(2), 221–259. https://doi.org/10.1016/j.neuron.2016.05.039
53. Ache, J. M., & Dürr, V. (2015). A computational model of a descending mechanosensory pathway involved in active tactile sensing. *PLOS Computational Biology*, *11*(7), e1004263. https://doi.org/10.1371/journal.pcbi.1004263
54. Mohren, T. L., Daniel, T. L., Brunton, S. L., & Brunton, B. W. (2018). Neural-inspired sensors enable sparse, efficient classification of spatiotemporal data. *Proceedings of the National Academy of Sciences of the United States of America*, *115*(42), 10564–10569. https://doi.org/10.1073/pnas.1808909115
55. Newman, B. G., Savage, S. G., & Schouella, D. (1977). Model tests on a wing section of an Aeschna dragonfly. In T. J. Pedley (Ed.), *Scale Effects in Animal Locomotion*.
56. Weller, H. G., Tabor, G., Jasak, H., & Fureby, C. (1998). A tensorial approach to computational continuum mechanics using object-oriented techniques. *Computers in Physics*, *12*(6), 620–631. https://doi.org/10.1063/1.168744
57. Community, B. O. (2018). *Blender—A 3D modelling and rendering package (3.v.1)*. Stitching Blender Foundation. http://www.blender.org
58. Schindelin, J., Arganda-Carreras, I., Frise, E., Kaynig, V., Longair, M., Pietzsch, T., Preibisch, S., Rueden, C., Saalfeld, S., Schmid, B., Tinevez, J. Y., White, D. J., Hartenstein, V., Eliceiri, K., Tomancak, P., & Cardona, A. (2012). Fiji: An open-source platform for biological-image analysis. *Nature Methods*, *9*(7), 676–682. https://doi.org/10.1038/nmeth.2019
59. Ahrens, J., Geveci, B., & Law, C. (2005). *ParaView: An end-user tool for large data visualization*. Elsevier.
60. Team, R. (2020). *RStudio: Integrated Development for R (5.10)*. RStudio, PBC. http://www.rstudio.com/
61. Dieck, R. H. (2007). Uncertainty (error) propagation. In *Measurement uncertainty: Methods and applications* (4th rev. ed., pp. 111–146). ISA.
62. Tuthill, J. C., & Wilson, R. I. (2016). Mechanosensation and adaptive motor control in insects. *Current Biology*, *26*(20), R1022–R1038. https://doi.org/10.1016/j.cub.2016.06.070
63. Wang, L., Liang, P.-J., Zhang, P.-M., & Qiu, Y.-H. (2014). Ionic mechanisms underlying tonic and phasic firing behaviors in retinal ganglion cells. *Channels*, *8*(4), 298–307. https://doi.org/10.4161/chan.28012
64. Project, I. (2020). Inkscape (1.01). https://inkscape.org
65. Gracey, W. (1958). Summary of methods of measuring angle of attack on aircraft. Technical Note 4351. National Advisory Committee for Aeronautics.
66. Sankaralingam, L., & Ramprasadh, C. (2020). A comprehensive survey on the methods of angle of attack measurement and estimation in UAVs. *Chinese Journal of Aeronautics*, *33*(3), 749–770. https://doi.org/10.1016/j.cja.2019.11.003
67. Dickinson, M. H., Lehmann, F. O., & Sane, S. P. (1999). Wing rotation and the aerodynamic basis of insect right. *Science*, *284*(5422), 1954–1960. https://doi.org/10.1126/SCIENCE.284.5422.1954
68. Anwer, S. F., Ashraf, I., Mehdi, H., Ahmad, A., & Grafi, H. (2013). On the aerodynamic performance of dragonfly wing section in gliding mode. *Advances in Aerospace Science and Applications*, *3*(3), 227–234.
69. Thurm, U. (1963). Die Beziehungen zwischen mechanischen Reizgrössen und stationären Erregungszuständen bei Borstenfeld-Sensillen von Bienen. *Zeitschrift Für Vergleichende Physiologie*, *46*(4), 351–382. https://doi.org/10.1007/BF00340465
70. Nicklaus, R. (1965). Die Erregung einzelner Fadenhaare von Periplaneta americana in Abhängigkeit von der Grösse und Richtung der Auslenkung. *Zeitschrift Für Vergleichende Physiologie*, *50*(4), 331–362. https://doi.org/10.1007/BF00339423
71. Bowers, A. H., Murillo, O. J., Jensen, R. R., Eslinger, B., & Gelzer, C. (2016). On wings of the minimum induced drag: Spanload implications for aircraft and birds.
72. Combes, S. A., & Daniel, T. L. (2003). Flexural stiffness in insect wings I. Scaling and the influence of wing venation. *Journal of Experimental Biology*, *206*(17), 2979–2987. https://doi.org/10.1242/jeb.00523
73. Combes, S. A., & Daniel, T. L. (2003). Flexural stiffness in insect wings II. Spatial distribution and dynamic wing bending. *Journal of Experimental Biology*, *206*(17), 2989–2997. https://doi.org/10.1242/jeb.00524
74. Chen, L., Wu, J., & Cheng, B. (2020). Leading-edge vortex formation and transient lift generation on a revolving wing at low Reynolds number. *Aerospace Science and Technology*, *97*, 105589. https://doi.org/10.1016/j.ast.2019.105589
75. Dickerson, B. H., Fox, J. L., & Sponberg, S. (2021). Functional diversity from generic encoding in insect campaniform sensilla. *Current Opinion in Physiology*, *19*, 194–203. https://doi.org/10.1016/j.cophys.2020.11.004
76. Hou, D., & Zhong, Z. (2022). Comparative analysis of deformation behaviors of dragonfly wing under aerodynamic and inertial forces. *Computers in Biology and Medicine*, *145*, 105421. https://doi.org/10.1016/J.COMPBIOMED.2022.105421
77. Zheng, L., Wang, X., Khan, A., Vallance, R. R., Mittal, R., & Hedrick, T. L. (2009). A combined experimental-numerical study of the role of wing flexibility in insect flight. *47th AIAA Aerospace Sciences Meeting Including the New Horizons Forum and Aerospace Exposition*. https://doi.org/10.2514/6.2009-382
78. Bai, S., & Luo, S. (1991). Theoretical and computational dynamics of a compressible flow. *NASA STI/Recon Technical Report A*, *92*, 26775.
79. Jennings, S. G. (1988). The mean free path in air. *Journal of Aerosol Science*, *19*(2), 159–166. https://doi.org/10.1016/0021-8502(88)90219-4
80. Gherlone, M., Cerracchio, P., & Mattone, M. (2018). Shape sensing methods: Review and experimental comparison on a wing-shaped plate. *Progress in Aerospace Sciences*, *99*, 14–26. https://doi.org/10.1016/j.paerosci.2018.04.001

SUPPORTING INFORMATION

Additional supporting information can be found online in the Supporting Information section at the end of this article.

How to cite this article: Uhrhan, M. J., Bomphrey, R. J., & Lin, H.-T. (2024). Flow sensing on dragonfly wings. *Ann NY Acad Sci.*, *1536*, 107–121. https://doi.org/10.1111/nyas.15152